Sensors and Actuators B 161 (2012) 235–243

Contents lists available at SciVerse ScienceDirect

Sensors and Actuators B: Chemical

journal homepage: www.elsevier.com/locate/snb

All photonic bandgap fiber spectroscopic system for detection of refractive index changes in aqueous analytes

Hang Qu, Bora Ung, Mathieu Roze, Maksim Skorobogatiy*

Genie physique, Ecole Polytechnique de Montreal, C.P.6079, Succ, Centre-ville, Montreal, QC, Canada H37 3A7

ARTICLE INFO

Article history:
Received 21 May 2011
Received in revised form 4 October 2011
Accepted 12 October 2011
Available online 3 November 2011

Keywords:
Photonic crystal fiber
Bragg fiber sensor
Fiber-optic sensor

ABSTRACT

We propose and experimentally demonstrate a sensor of refractive index (RI) of aqueous analytes based on a hollow-core low-refractive-index-contrast Bragg fiber. Variations in refractive index of liquid analytes filling the hollow core of Bragg fiber could modify the resonant condition of the modal confinement, thus leading to both spectral shifts and intensity changes in the fiber transmission. As a proof-of-principle demonstration, we characterize sensor performance using a set of NaCl solutions with different concentrations. The experimental sensitivity of the Bragg fiber sensor is found to be ~1400 nm/RIU (refractive index unit), which is comparable to those of surface plasmon resonance sensors. Moreover, we demonstrate the integration of a Bragg fiber bundle spectrometer in the liquid-core Bragg fiber sensing system to replace the grating-based monochromator, which could potentially lead to significant cost-saving and increased sensing speed. In summary, we demonstrate an all-photonic-bandgap-fiber RI sensing system that uses a hollow core Bragg fiber to hold and probe the analyte, and a solid-core Bragg fiber bundle for spectral interpretation of the transmitted light.

© 2011 Elsevier B.V. All rights reserved.

1. Introduction

Recently, liquid-core waveguides have drawn much attention for chemical and biological sensing applications. A typical liquid-core waveguide sensor operates on the principle of total internal reflection (TIR) where liquid core is surrounded by the lower refractive index (RI) cladding [1]. Unfortunately, the difficulty in finding suitable cladding material with the refractive index lower than those of aqueous solutions ($n \sim 1.33$) limits TIR liquid-core sensor development. One way to circumvent this problem is to use the "leaky modes" guided in the low-RI core surrounded by the high-RI cladding. This is an approach used by the liquid- and air-core capillary sensors reported in [2,3]. These capillary sensors, however, have limited sensing length due to large propagation loss, and are mainly used to detect imaginary parts of analyte RIs.

Using sensors based on hollow-core (HC) photonic crystal fibers (PCFs) constitutes an alternative to capillary sensors. Most of HC-PCF sensors guide by bandgap effect according to which the light within a certain frequency (reflector bandgap) is confined in the fiber core. The propagation loss is determined by the core material absorption and fiber radiation losses. Compared to capillary sensors, HC-PCF sensor enables longer sensing length, while having virtually complete light-analyte overlap throughout the entire fiber length, which makes HC-PCF sensors potentially more advantageous in detecting imaginary part of the analyte RI. Besides, HC-PCF sensors could be also used to detect real part of the analyte RI, as well as other measurands that could affect resonant conditions of the HC-PCFs. Up to date, HC-PCF based sensors have already been used for sensing of real and imaginary parts of RIs of liquid or gas analytes [4–20], as well as sensing of temperature, strain, pressure [21–23], etc. These HC-PCF based sensors are summarized in Table 1.

Particularly, as to sensing of liquid analytes, most of the previously reported HC-PCF sensors operate on the following three configurations.

Firstly, as to detection of real parts of analyte RIs, most of liquid-core PCF sensors use a resonant sensing mechanism according to which the transmission spectrum of the liquid-core PCF shifts in response to variations in RI of the liquid analyte filling the fiber core. For example, in [4,5] the liquid RI sensor based on a commercial glass PCF is reported with the sensitivity found to be on order of $\sim 5 \times 10^3$ nm/RIU. A relative long time is needed to fill a liquid analyte into the micron-sized holes of the PCF (~10 min/20 cm reported in [4]). Another example of the sensor uses the HC high-RI-contrast Bragg fiber [6] which shows a tunable bandgap when changing RI of the liquid analyte filling the fiber core. However, the high-RI-contrast Bragg fiber sensor is mainly used to detect high-RI analytes ($n_{analyte} > 1.40$ in [6]), while it becomes somewhat problematic when measuring low-RI analytes including aqueous solutions ($n_{analyte} \sim 1.33$) as we will explain in Section 2.

* Corresponding author.
E-mail address: maksim.skorobogatiy@polymtl.ca (M. Skorobogatiy).

0925-4005/$ – see front matter © 2011 Elsevier B.V. All rights reserved.
doi:10.1016/j.snb.2011.10.025

Table 1
HC-PCF based sensors.

HC-PCF based sensor	Sensing mechanism	Wavelength	Sensitivity	Ref.
Liquid analyte sensing				
•Liquid RI sensing	Resonant sensing ($Re(n_a)$ sensing)	600–1700 nm	~5000 nm/RIU	[4,5]
		400–900 nm	~300 nm/RIU	[6]
•Bio-sensing	Evanescent field sensing ($Im(n_a)$ sensing)	500–600 nm	-	[7]
		500–760 nm	-	[8]
•Chemical sensing	Raman scattering sensing	500–4000 cm^{-1}	1.7×10^{-7}M (molarity)	[9]
		600–2000 cms^{-1}	10^{-4}–10^{-5}M	[10]
		500–2000 cm^{-1}	~10^{-3}M	[11]
		600–1800 cm^{-1}	10^{-10}M	[12]
Gaseous analyte sensing	Gas specific absorption sensing ($Im(n_a)$ sensing)	7–14 μm	30 ppb (parts per billion)	[13]
		1000–7000 cm^{-1}	-	[14]
		1000–1700 nm	-	[15]
		1550–1640 nm	647 ppm (parts per million)	[16]
		1630–1680 nm	10 ppm	[17]
		1200–1600 nm	49 ppm	[18]
	Raman scattering sensing	500–600 nm	-	[19]
		865–900 nm	-	[20]
Temperature sensing	Resonant sensing: bandgap shift detection	1500–1750 nm	29 nm/°C	[21]
		1200–1600 nm	3.97 pm/°C	[22]
		1500–1660 nm	0.86 pm/°C	[23]
Strain/pressure sensing	Resonant sensing: bandgap shift detection	1500–1750 nm	−0.7 pm/με	[21]
		1200–1600 nm	−0.81 pm/με	[22]
		1500–1660 nm	0.6 pm/με	[23]

Note: The fiber used in Refs. [6,13,14] is the HC high-RI-contrast Bragg fiber. In other papers, the fiber used for sensing is the HC photonic bandgap fiber featuring a center hollow core surrounded by periodical microscopic holes. $Re(n_a)$ and $Im(n_a)$ are the real part and imaginary part of the analyte RI, respectively.

Secondly, the liquid-core PCFs can be used as "multi-core" waveguide sensors operating on the evanescent-field sensing principle [7,8]. While each node of the struts in the microstructured cladding forms a "core", the PCF is used as a "multi-core" waveguide rather than a photonic bandgap (PBG) fiber. Fluorophore-labeled analytes are then probed by the evanescent field penetrating from the "cores" into the liquid-filled holes. The sensitivity of the sensor is limited by the small overlap between analytes and the evanescent field in the micron-sized holes. Reported response time is also long (several minutes) due to the slow process of filling analytes into the micron-sized holes.

Thirdly, another implementation of the liquid-core PCF sensor involves using normal or surface-enhanced Raman scattering in the partially filled HC-PCFs [9–12]. In such a sensor, a selective infiltration technique is used to fill liquid analytes only in the center hole of a PCF, which will enhance the light confinement of the fiber due to the increased RI-contrast between the center liquid-filled core and the air-filled microstructured cladding. The selectively filled PCF, therefore, guides by a modified index-guiding mechanism, and the Raman signal from liquid analytes in the fiber core is detected. The detection limit of the PCF based Raman sensor could be on order of 10^{-10} M [12]. Main challenge of this technique is in the selective filling step which considerably complicates fabrication of the PCF sensor.

The goal of this paper is to demonstrate a liquid-core low-RI-contrast Bragg fiber sensor (Fig. 1) which is used for detection of real part of liquid RIs. The sensor operates on a resonant sensing principle in which variations in real part of the analyte RI filling the Bragg fiber core lead to both intensity changes and spectral shifts in the fiber transmission [24]. Experimental sensitivity of sensor is found to be ~1400 nm/RIU. We also show that the sensitivity of the liquid-core Bragg fiber sensor is virtually independent on the length of the fiber. The response time of the sensor using an 80 cm long fiber is ~1 s, which represents an advantage compared to the previously reported liquid-core PCF sensors (response time ~10 min). Besides, we note that low-RI-contrast Bragg fibers show good guidance when filled with aqueous solutions. However, high-RI-contrast Bragg fibers have the TM (transverse magnetic) bandgaps that tend to collapse in the vicinity of the light line of water because of the Brewster angle phenomenon. Thus, high-RI-contrast Bragg fibers have relatively poor guidance of the hybrid modes propagating in an aqueous core, which cause the difficulty of sensing aqueous analytes.

In this paper, we also demonstrate the integration of a Bragg fiber bundle spectrometer in the liquid-core Bragg fiber sensing system. The Bragg fiber bundle spectrometer, reported in [25] has shown high accuracy in detecting the center peak position of a test spectrum, which can be used to analyze transmission peak shifts of a liquid-core Bragg fiber. Using the Bragg fiber bundle spectrometer potentially allows forgoing traditional grating-based spectrometers, thus leading to significant cost-saving and increased sensing speed. Besides, unlike the grating-based spectrometer with the resolution dependent on spatial line density of the grating and length of the optical path inside the spectrometer, the fiber bundle spectrometer has a resolution independent on the fiber bundle length. Therefore, a highly compact all-PBG-fiber based liquid RI sensor could be constructed by using a several-centimeter-long fiber bundle connected to a coiled HC Bragg fiber. To the best of our knowledge, this is the first time when a complete liquid-core RI fiber-optic sensor has been demonstrated where both the sensing cell and the spectrometer are realized using hollow- and solid-core PBG fibers.

2. Operation principle of liquid-core Bragg fiber sensor

The all-polymer HC low-RI-contrast Bragg fiber used in the sensor is fabricated in our group [26]. This Bragg fiber features a large air core (diameter: ~0.8 mm) surrounded by an alternating polymethyl methacrylate (PMMA)/polystyrene (PS) Bragg reflector (RI: 1.487/1.581 @ 589 nm) and a PMMA cladding (Fig. 1(b)). The large core of the Bragg fiber facilitates filling it with aqueous solutions which might even contain some large objects. Such a large core also leads to a short response time of the sensor, since the flow resistance in the core decreases polynomially as the core radius increases. Experimentally, response time of a sensor using an 80 cm long fiber is found to be ~1 s.

The guiding and sensing properties of the low-RI-contrast Bragg fiber can be elucidated from the Bragg reflector band diagram

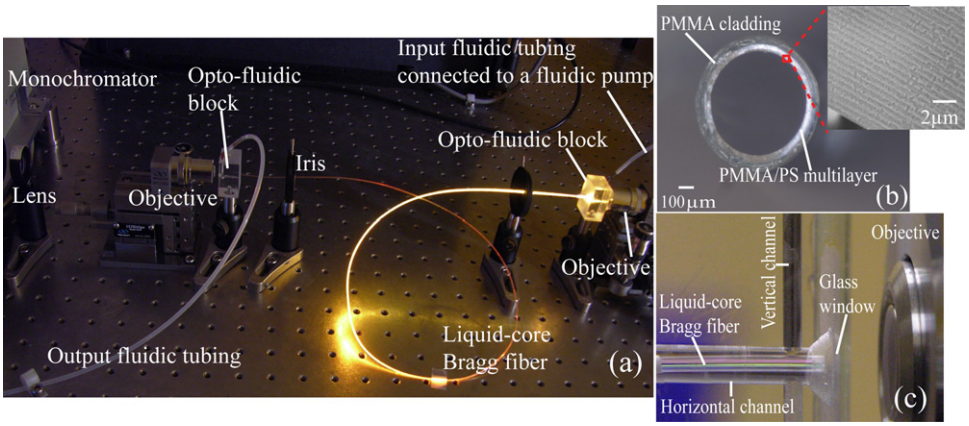

Fig. 1. (a) Setup of the Bragg fiber sensing system. An 80 cm long liquid-core Bragg fiber, coiled into a ~15 cm diameter circle, is integrated in the setup by using two opto-fluidic coupling blocks. The beam from a supercontinuum source is coupled into the liquid-core Bragg fiber, and the transmission spectrum of the liquid-core Bragg fiber is then analyzed by a traditional grating monochromator. (b) Cross section of a HC Bragg fiber; the inset is the graph of the Bragg reflector taken by a scanning electron microscope (SEM). (c) Inner structure of the opto-fluidic block. A tip of a liquid-core Bragg fiber is sealed in the horizontal channel of the block filled with the liquid analyte. The extremity of the horizontal channel is sealed by a glass window through which the light is coupled into (or out of) the sensing system. In each block there is also a vertical channel that connects to the horizontal channel to constitute the fluidic path for fluidic coupling of the Bragg fiber. The colorful appearance of the Bragg fiber is due to the reflection of ambient lights from the Bragg reflector. (For interpretation of the references to color in this figure legend, the reader is referred to the web version of this article.)

(frequency versus propagation constant). In Fig. 2, we show the band diagram of the TE (transverse electric) and TM polarized modes propagating in an infinite planar Bragg reflector made from PMMA/PS multilayer. To make the band diagram, we measure the refractive indices of PMMA and PS with a VASE Ellipsometer (J.A. Woollam Co., Inc.). The average thicknesses of the individual PMMA and PS layers are 0.37 μm and 0.13 μm, respectively, estimated from the SEM graphs. Grey regions in Fig. 2 indicate states delocalized over the whole Bragg reflector. Such states are efficiently irradiated out of the fiber due to scattering on the imperfections in the multilayer. Clear regions (bandgaps) define the parts of the phase space where light is forbidden to propagate inside of the Bragg reflector. The black thick curves represent the light line of the liquid analyte, i.e. distilled water. Modes guided in the hollow core will have effective RIs close to, while somewhat smaller than that of water (black thick curves in Fig. 2). Therefore, a mode confined in the liquid core will exist in the regions of a band diagram where light lines of water intersect the reflector bandgap (horizontal green regions in Fig. 2)

From the basic theory [27] of low-RI-contrast Bragg fibers, the center wavelength, λ_c, of the fundament reflector bandgap can be approximately calculated by:

$$\frac{\lambda_c}{2} = d_h(n_h^2 - n_c^2)^{1/2} + d_l(n_l^2 - n_c^2)^{1/2} \quad (1)$$

where d_l, d_h are thicknesses of the low- and high-index layer, respectively; n_l, n_h are real parts of RIs of the corresponding layers; n_c is real part of RI of the core material. Variations in real part of the analyte RI filling the core could modify the resonant condition (1) of the Bragg fiber, thus resulting in spectral shifts of the resonant wavelength in the fiber transmission, which constitutes the main sensing principle of the Bragg fiber sensor.

We note that low-RI-contrast Bragg fibers have certain advantages for liquid analyte sensing compared to their high-RI-contrast counterparts. Previously, high-RI-contrast Bragg fibers have been used for sensing of gas analytes ($n_{analyte} \sim 1$) [13], as well as liquid analytes with high refractive indices ($n_{analyte} > 1.40$) [6]. However, for the high-RI-contrast Bragg fibers used in these works, the TM

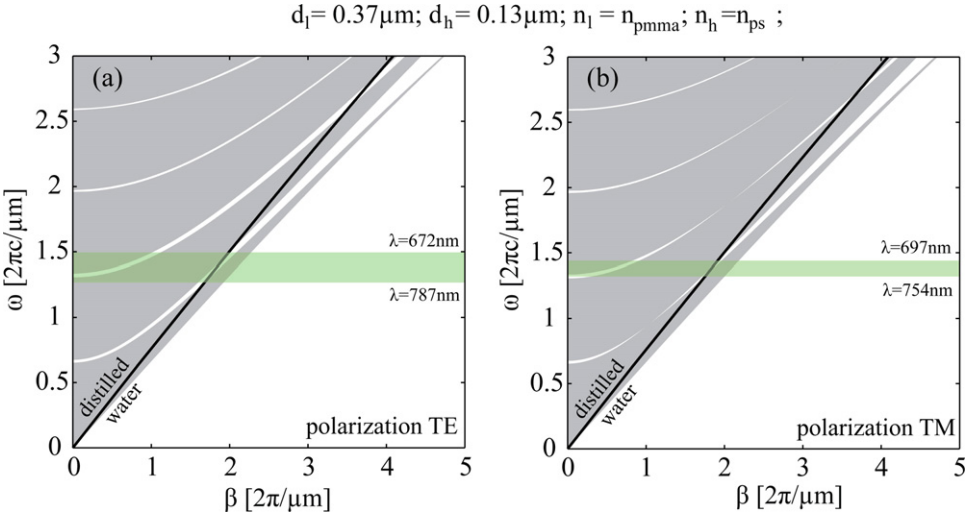

Fig. 2. Band diagram of (a) TE and (b) TM polarized modes of a PMMA/PS Bragg reflector. The grey regions corresponds to (β, ω) for which light can propagate within the Bragg reflector. The clear regions correspond to the parts of phase space where light is forbidden to propagate in the Bragg reflector. Thick black curves represent the light line of distilled water. Transmission bands (green) of the Bragg fiber can be estimated from the intersection of light line of water with the Bragg reflector bandgaps. (For interpretation of the references to color in this figure legend, the reader is referred to the web version of this article.)

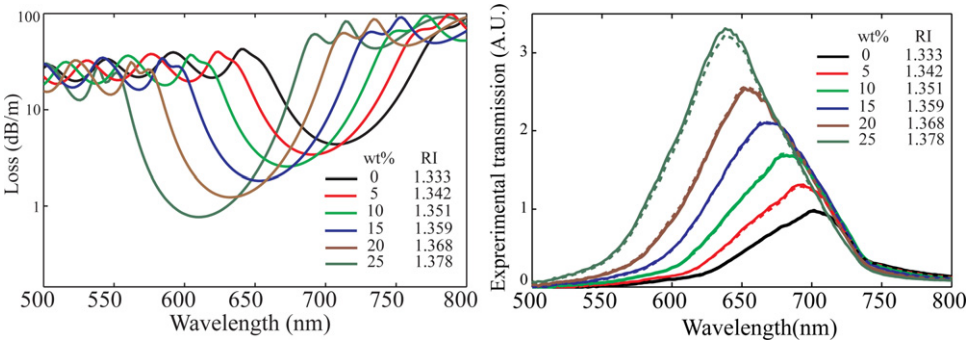

Fig. 3. (a) Simulated loss of the fundamental mode (HE_{11} mode) of the Bragg fiber filled with different NaCl solutions. (b) Experimental transmission spectra of the ~40 cm long Bragg fiber filled with NaCl solutions (solid curves). The dotted curves indicate a repeat of the first experiment after several hours, which demonstrate a good repeatability of the measurement. The weight concentrations (wt.%) and the RIs of the NaCl solutions are listed in both figures as insets.

bandgaps of the Bragg reflector tend to collapse near the light line of the aqueous material ($n_{analyte} \sim 1.33$) due to the Brewster angle phenomenon, thus leading to high loss for the hybrid (HE/EH) modes propagating in the liquid cores. In contrast, low-RI-contrast Bragg fibers show large TM bandgaps in the vicinity of the light line of water, thus resulting in good guidance of HE/EH modes (Fig. 2). Moreover, we note that low-RI-contrast Bragg fibers are more sensitive to changes in RI of liquid analytes filling the fiber core, as compared to high-RI-contrast Bragg fibers. Particularly, from Eq. (1), we derive the sensitivity of the sensor, S, as:

$$S = \frac{d\lambda_c}{dn_c} = 2\left[d_h\left(\frac{n_h^2}{n_c^2} - 1\right)^{-1/2} + d_l\left(\frac{n_l^2}{n_c^2} - 1\right)^{-1/2}\right] \quad (2)$$

According to Eq. (2), the closer is the value of the core RI to those of the individual layers of the Bragg reflector; the more sensitive the Bragg fiber sensor will be to variations in RI of the analyte-filled core, which is exactly the case for our low-RI-contrast Bragg fiber sensor.

3. Simulation and experiments

To verify the resonant sensing mechanism theoretically, we simulate the loss spectra of the fundamental mode (HE_{11} mode) of the liquid-core Bragg fiber based on the Transfer Matrix Method (TMM) [28]. The structural parameters of the HC Bragg fiber are same as those used in Section 2. As liquid analytes, we choose a set of NaCl solutions with the weight concentration ranging from 0 to 25% with a 5% increment step. The corresponding RIs of NaCl solutions are shown in Fig. 3 [29]. The bulk absorption of NaCl solutions in the spectral range of interest was shown to be virtually identical with that of pure water [30]. In our simulations, we, therefore, compute a propagation loss of an HE_{11} mode taking into account absorption loss of water, as well as dispersion of water and plastics in the Bragg reflector. The simulated loss spectra suggest that the transmission band of the liquid-core Bragg fiber shows a blue-shift as the RI of the liquid analyte increases (Fig. 3(a)).

In our experiments, we employ two opto-fluidic blocks designed to simultaneously enable optical and fluidic coupling of the HC fiber (Fig. 1). A ~40 cm long Bragg fiber, coiled into a 10 cm diameter circle, is integrated into the sensing system. On each side, the HC Bragg fiber tip is inserted hermetically into the analyte-filled horizontal channel that has a thin glass window attached at the one of its extremities for optical coupling of the Bragg fiber (Fig. 1(c)). In each block there is also a vertical channel which connects to the horizontal channel to constitute the fluidic path for fluidic coupling of the Bragg fiber. This design avoids formation of air bubbles in the sensing system which would strongly suppress fiber transmission. After pumping a liquid analyte into the fiber, we couple the beam from a supercontinuum source into the fiber using a 10× objective, and the transmission spectrum of the liquid-core Bragg fiber is then analyzed by the Newport grating monochromator. To verify the repeatability of the sensor, we have repeated the same experiment after 3 h by first purging the setup with distilled water. Fig. 3(b) shows the result of two consecutive experiments. The solid curve represents transmission spectrum of the first measurement, and it compares well with the second measurement shown as the dotted curve. We observe up to no more than 2.51% fluctuation in the detected intensity, while the center position of the transmission peak stays at the same position up to the resolution limit (~1 nm) of our spectrometer. As seen in Fig. 3(b), the experimental transmission spectrum also features a blue-shift as the RI of the NaCl solution filling the core increases. Moreover, the spectral shifts of the transmission peak show a linear dependence on the increasing refractive index of the analyte filling the core (Fig. 4).

We note that the experimental spectral shifts of a fiber transmission peak are somewhat smaller than the simulated ones. This is likely due to the fact that in our simulation we only calculate the spectral shifts of the fundamental (HE_{11}) mode with effective RI identical to that of the liquid analyte filling the core. Virtually, most higher-order core modes have effective RIs (n_{eff}) lower than that of the HE_{11} mode. Therefore, by substitution of n_c by n_{eff} in Eq. (2), we arrive to the conclusion that spectral shifts of the transmission peaks of higher-order modes are smaller than those of the HE_{11} mode. Due to large diameter of the Bragg fiber core used in the experiments, many higher-order modes are excited. As these high-order modes are less sensitive than the HE_{11} mode, the experimental spectral shifts are, therefore, smaller than those of the HE_{11}

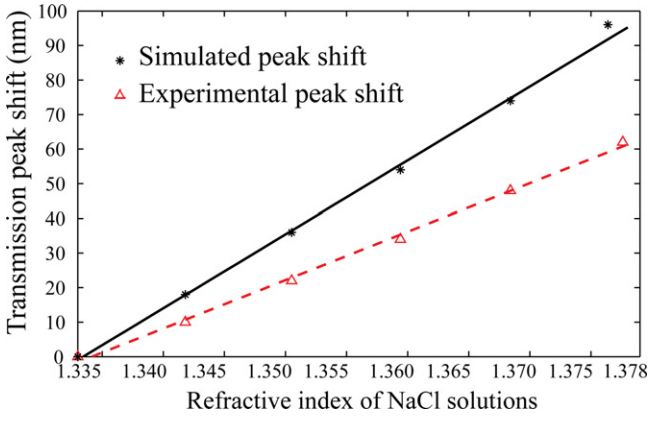

Fig. 4. Spectral shifts of the fiber transmission peak obtained from the TMM simulation (black solid line) and the experimental measurements (red dash line). (For interpretation of the references to color in this figure legend, the reader is referred to the web version of this article.)

mode. Finally, from Fig. 4, we conclude that the experimental sensitivity of the liquid-core Bragg fiber sensor is ~1400 nm/RIU. Such a sensitivity is comparable to those of previous MOF based sensors [4,5,31,32], but is an order smaller than that of the dual-core MOF sensor with a sensitivity of ~30,000 nm/RIU [33]. However, we note that the dual-core MOF sensor is limited to be used for sensing liquid analytes with $n_{analyte} > n_{silica}$. In addition, compared to other MOF based sensors, our Bragg fiber sensor is advantageous in its short response time (~1 s) due to the large core of the Bragg fiber.

4. Discussion of factors influencing sensor performance

4.1. Dynamic range of the sensor

The choice of the operation frequency range is mainly determined by the position of the Bragg reflector bandgap. Currently, we routinely produce Bragg fibers with primary bandgaps located in 500–800 nm spectral range; therefore, all our experiments are conducted in this range. Sensitivity of the sensor is so high that with varying the liquid-core RI from 1.333 to 1.378, the fiber bandgap already spans this whole operational window (see Fig. 3). From band diagram of Fig. 2, it follows that the largest wavelength of operation is $\lambda \sim 1300$ nm. That is the region where sensing of low-RI analytes with $n_{eff} \sim 0$ can be achieved. In application to aqueous analytes, the bulk absorption is generally larger than 50 dB/m at the wavelength above 1 μm, thus limiting the operation range of the sensor in the near-infrared range. Finally, for the high RI analytes the fiber bandgap will shift into blue spectral region; however, there is no fundamental limit for the use of these sensors for high-RI analytes.

4.2. Insertion and coupling loss

Due to the large diameter of the Bragg fiber core (over 0.5 mm), coupling efficiency of the fiber is superb (above 90%), which is one of the well known advantages of such fibers. Main coupling loss of the sensor comes from the reflection between the air and the glass window covering the fluidic channel (Fig. 1(c)). The total coupling and out-coupling loss is estimated to be ~10%.

4.3. Dependence of sensitivity on fiber length

To study the dependency of the sensitivity on the length of Bragg fiber, we first measure the transmission spectral shifts of a 50 cm long Bragg fiber filled with NaCl solutions of different concentrations. Then, we cut the fiber into 30 cm and 20 cm, and for each length we repeat the experiment to measure the spectral shifts in response to variations in the liquid-core RI. In Fig. 5, we plot fiber transmission spectra of liquid-core Bragg fiber with different lengths.

The transmission spectra of the 50 cm long Bragg fiber show clear spectral shifts caused by variations in the core RI (Fig. 5(a)). The sensitivity of the 50 cm long fiber sensor is ~1300 nm/RIU which is estimated from the spectral shifts of the specific transmission peak marked by white arrows. In the transmission spectra of the 30 cm long Bragg fiber, we still observe spectral shifts of the transmission peak (Fig. 5(b)); however, the transmission spectra become broader due to reduced fiber attenuation at the bandgap edges because of shorter fiber length. The experimental sensitivity of the 30 cm long Bragg fiber sensor is ~1270 nm/RIU (Fig. 5(d)). Further reduction of the Bragg fiber length to 20 cm leads to even smaller propagation losses at all frequencies. However, the reduced fiber loss causes the difficulty in differentiating specific resonant features in the fiber transmission spectra, and as a result it becomes difficult to detect spectral shifts.

Therefore, we conclude that the liquid-core Bragg fiber should have a minimal (threshold) length to ensure sufficient attenuation at the wavelengths in the vicinity of bandgap edges in order to allow formation of spectral features (such as transmission peaks) in the fiber transmission. We experimentally find the threshold length to be ~10 cm for most Bragg fibers used in our experiments. Once the fiber length is longer than the threshold value, the sensitivity of a Bragg fiber sensor does not strongly depends on the fiber length, which is consistent with the prediction in [24]. Longer fiber also leads to a stronger attenuation of the higher-order modes, thus acting as a high-order mode striper, which is also beneficial for sensing. At the same time, signal strength in longer fibers decreases due to increased material absorption and radiation losses, eventually leading to signal-to-noise degradation, which is disadvantageous for sensing. It is the trade-off between the two above-mentioned factors that determine the optimal fiber length. Note that the optimization of the sensing length is not strictly required for sensing applications. Experimentally, we found the maximal sensing length of Bragg fiber to be ~1 m. With the sensing length smaller than ~1 m, one can always measure the transmission spectrum of Bragg fiber without much signal-to-noise degradation. Therefore, when sensing a specific liquid analyte, one, in practice, could choose the Bragg fiber with any length between the threshold value (~10 cm) and the maximal length (~1 m).

5. Liquid-core Bragg fiber sensor integrated with Bragg fiber bundle spectrometer

5.1. Bragg fiber bundle spectrometer

Recently, we demonstrated that the function of a spectrometer can be implemented in a solid-core Bragg fiber bundle [25]. The solid-core Bragg fiber bundle spectrometer breaks the paradigm of a traditional spectrometer in which the resolution is directly related to the length of the light path inside the spectrometer and the line density of the Bragg grating used. Instead, the Bragg fiber bundle spectrometer relies on the ability of Bragg fibers to filter a particular spectral window of the incoming light. The test spectrum can be reconstructed by interrogating transmitted intensities in the individual Bragg fibers in the bundle and then by applying a deconvolution algorithm to these intensities with a "transmission matrix" method. We have experimentally demonstrated that the Bragg fiber bundle spectrometer can reconstruct the center peak position of a test spectrum within several percent of its true value for a large range of the peak widths and positions. In this context, it is interesting to investigate the possibility of designing an all-PBG fiber based spectroscopic system where the function of sensing cell and spectrometer are implemented in the all fiber configuration. Ideally, one would splice the hollow core Bragg fiber with a spectrometric fiber to implement an integrated system with minimal requirements on the processing and acquisition equipment, thus reducing system cost and simplifying its maintenance.

Schematic of the Bragg fiber bundle spectrometer is shown in Fig. 6. The Bragg fiber bundle is fabricated using 100 solid-core Bragg fibers. Individual Bragg fibers have a large 300–800 μm diameter core made of PMMA. The core is surrounded by a Bragg reflector featuring a submicrometer-thick PMMA/PS multilayer. Note that guidance principles of the liquid-core Bragg fiber described above are also identical to those of the solid-core Bragg fiber, except that the core's RI of the latter is fixed. According to Eq. (1), thicknesses of the individual layers in the Bragg reflector determine center position of the transmission of a Bragg fiber. By choosing solid-core Bragg fibers with different transmission bands, we produce the Bragg fiber bundle which at the output has a mosaic

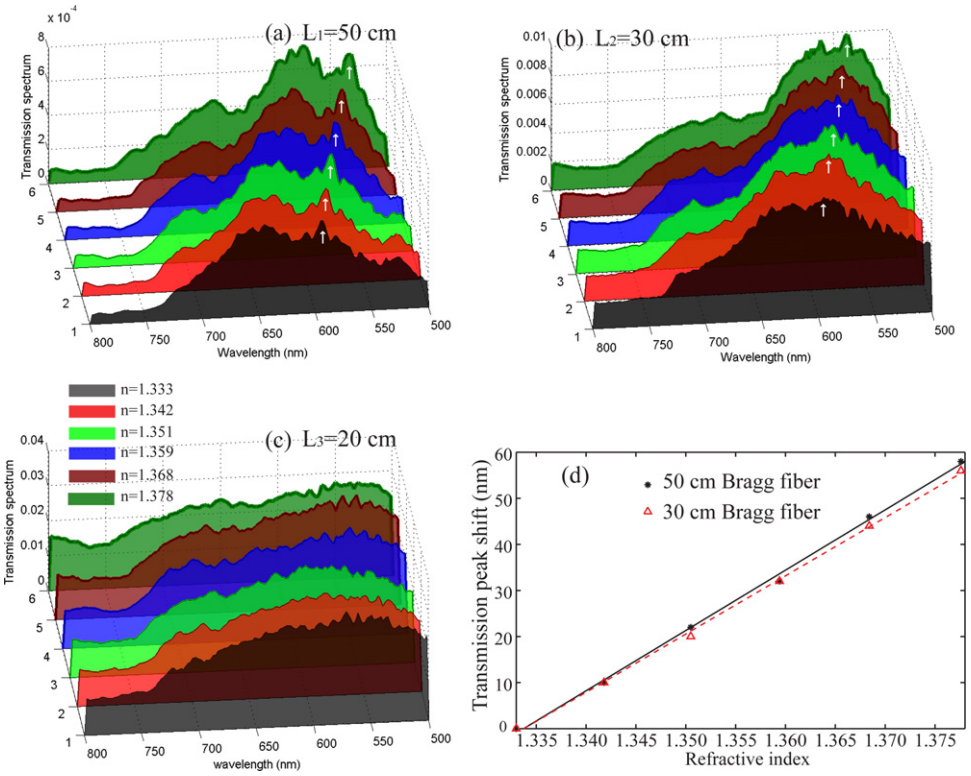

Fig. 5. Transmission spectra of the liquid-core Bragg fiber with different lengths: (a) 50 cm; (b) 30 cm; (c) 20 cm. The RIs of the analytes filling the fiber core are also listed in the inset of (c). The white arrows in (a) and (b) mark the resonant peak positions which we use to measure spectral shifts. A linear dependence of the spectral shifts on changes in RI of the fiber core is shown in (d). Black solid line represents the spectral shifts of a 50 cm long Bragg fiber and red dashed line represents the spectral shifts of a 30 cm long Bragg fiber. (For interpretation of the references to color in this figure legend, the reader is referred to the web version of this article.)

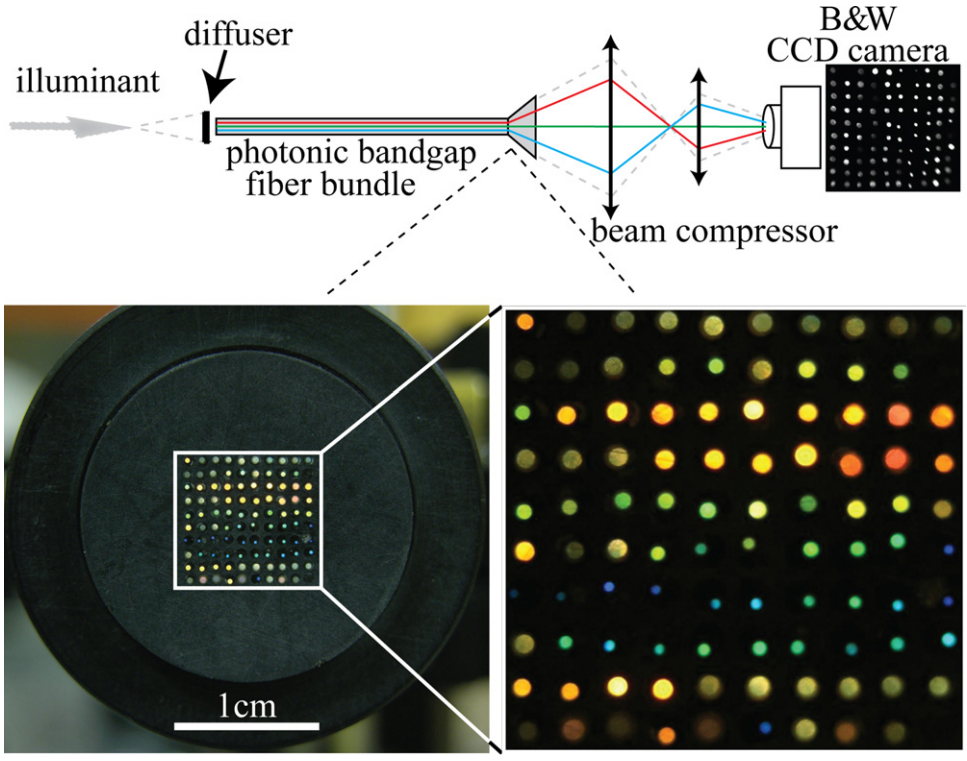

Fig. 6. Fiber bundle spectrometer [25]. Top, schematic of the spectrometer. The test spectrum is launched into the fiber bundle; output image of the fiber bundle is taken by a monochrome CCD camera. Bottom, when the broadband light is launched into the fiber bundle, the output is a mosaic of colors selected by the individual Bragg fibers. A beam compressor is used to ensure that the CCD camera accommodates the whole image of the output of Bragg fiber bundle. (For interpretation of the references to color in this figure legend, the reader is referred to the web version of this article.)

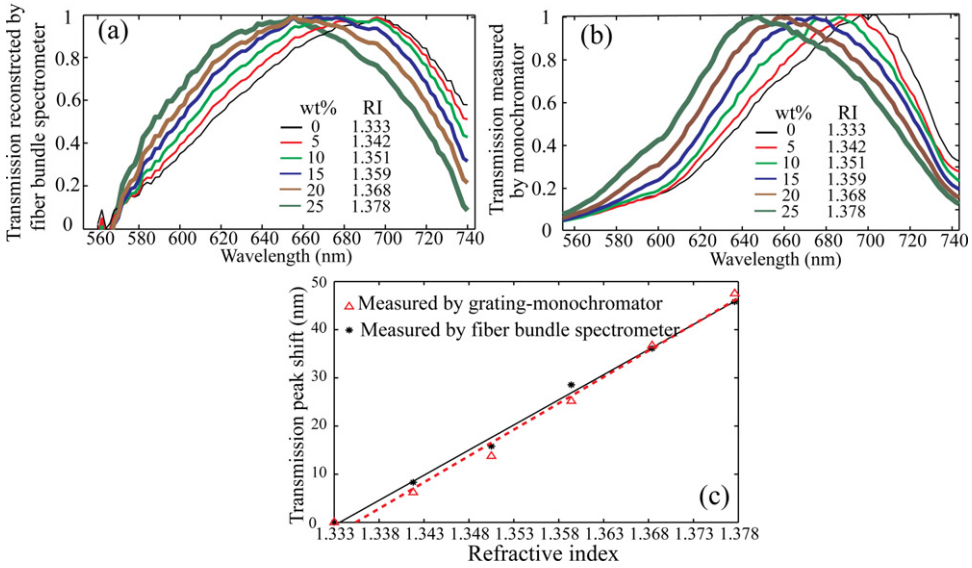

Fig. 7. Transmission spectra of the 40 cm long liquid-core Bragg fiber measured by (a) the Bragg fiber bundle spectrometer and (b) a conventional grating monochromator. The weight concentrations and the corresponding RIs of the NaCl solutions are listed in the inset. (c) Spectral shifts of the transmission peaks measured by the grating monochromator (dashed red line) and by the Bragg fiber bundle spectrometer (solid black line). (For interpretation of the references to color in this figure legend, the reader is referred to the web version of this article.)

of colors (bottom part of Fig. 6), when illuminated by white light.

An important factor that influences the performance of a Bragg fiber spectrometer is the intensity throughput which relates to the propagation losses of individual Bragg fibers in the fiber bundle. In practice, the typical propagation loss of an individual fiber in the 30 cm long bundle is ~3 dB of the light inside the bandgap and is 20 dB of the light outside the bandgap. Besides, transmission bands of the individual Bragg fibers in the bundle are relatively wide (60–180 nm FWHM) and partially overlapping. Because of these factors, the intensity throughput of an individual Bragg fiber is typically as much as 20% of the in-coupled light.

The operation principle of a Bragg fiber bundle spectrometer is described as follows. If transmission bands of the individual Bragg fibers are spectrally narrow and non-overlapping, the transmitted intensity of each fiber would be directly related to the corresponding spectral component of an incoming light. As a matter of fact, in our spectrometer the individual fiber bandgaps are strongly overlapping; we, therefore, use a deconvolution algorithm to reconstruct the test spectrum from the transmitted intensities of the Bragg fibers in the fiber bundle. Particularly, for a fixed exposure time of a CCD array, intensity C_n registered by the assigned region of a CCD camera corresponding to the output of the n_{th} fiber can be presented as:

$$C_n = \int_{\lambda_{\min}}^{\lambda_{\max}} I(\lambda) A_n F_n(\lambda) S(\lambda) O_n(\lambda) d\lambda \tag{3}$$

where $I(\lambda)$ is the incoming spectral flux density at the fiber bundle input end; A_n is the area of the n_{th} fiber input cross section; $F_n(\lambda)$ is the transmission function of the n_{th} fiber, $S(\lambda)$ is the spectral sensitivity of a CCD sensor; and $O_n(\lambda)$ is a fiber-position-dependent transmission function of various optics (diffuser, beam compressor). In Eq. (3), we can define a $T_n(\lambda) = A_n F_n(\lambda) S(\lambda) O_n(\lambda)$ to represent the transmission efficiency of the n_{th} fiber to transmit the in-coupled light to the CCD camera. In addition, we experimentally define the incoming spectrum in terms of small spectral intervals (bins) with equivalent width. We, then, use a matrix formalism to interpret the integral in (3) for all the Bragg fibers of the fiber bundle as

$$\begin{bmatrix} C_1 \\ \vdots \\ C_{100} \end{bmatrix} = \begin{bmatrix} T_{1,1} & \cdots & T_{1,N} \\ \vdots & \ddots & \vdots \\ T_{100,1} & \cdots & T_{100,N} \end{bmatrix} \begin{bmatrix} I_1 \\ \vdots \\ I_N \end{bmatrix} \tag{4}$$

where vector $(C)_{100\times 1}$ represents the intensities of light coming out the individual Bragg fibers as measured by the CCD camera; $(I)_{n\times 1}$ represents the discretized spectrum of the illuminant; $T_{(100\times n)}$ is a "transmission matrix" which denotes a linear conversion from the test spectrum (I vector) to the fiber transmitted intensities (C vector) measured by the CCD sensor. We calculate the matrix T through a calibration measurement demonstrated in the following section. From Eq. (4) the test spectrum can be reconstructed from the corresponding CCD image by inverting the "transmission matrix" of the Bragg fiber spectrometer. Note that due to strong overlap of the transmission spectra of the individual Bragg fibers in the bundle, the matrix T is ill-conditioned (even if made square). We, therefore, employ a standard singular value decomposition (SVD) method to calculate the pseudoinverse of the response matrix T to enable spectral reconstruction.

5.2. Calibration of the sensor integrated with the Bragg fiber bundle spectrometer

To calculate the response matrix T in Eq. (4), we carry out a calibration measurement for the Bragg fiber bundle spectrometer. We couple the beam of a supercontinuum source into a tunable monochromator (2 nm FWHM). Using a 10× objective, the output of the monochromator is then coupled into a 40 cm long Bragg fiber (from the same perform of the fiber used in Fig. 3) filled with distilled water. Since the output from the monochromator is relative weak, the water-filled Bragg fiber is kept straight during calibration measurement in order to reduce the propagation loss, thus increasing the signal-to-noise ratio of the measurement. Therefore, a supercontinuum-monochromator-Bragg-fiber (SMBF) source which has a tunable and quasi-monochromatic output is constructed. The SMBF source is then coupled to the Bragg fiber bundle spectrometer using another 10× objective. We

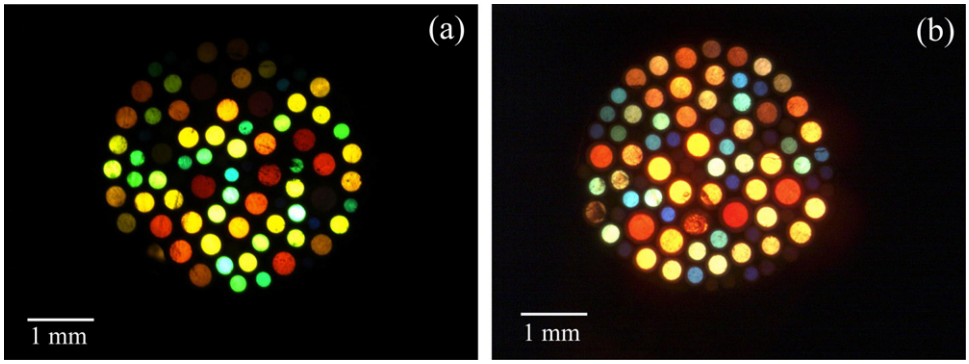

Fig. 8. Cross sections of fiber bundles drawn by the two-stage drawing technique. The bundle is illuminated with a broadband halogen lamp. At the output of fiber bundle, a mosaic of colors is visible as the white light is filtered by each fiber inside the bundle. (For interpretation of the references to color in this figure legend, the reader is referred to the web version of this article.)

vary the SMBF source center wavelength in 2 nm increments, thus effectively subdividing 560–750 nm spectral interval under consideration into $m = 96$ equivalent 2 nm wide bins. The SMBF source intensity, I_i, at each wavelength is also measured by the calibrated powermeter. For every position of the source center wavelength, we also acquire a C vector using the CCD array and consider it as a column of the response matrix of the Bragg fiber bundle spectrometer. By dividing every C vector by the corresponding I_i value, the transmission matrix T is constructed. After we calculate the matrix T, we can reconstruct a test spectrum by inverting T according to Eq. (4). We then remove the monochromator from the calibration setup and directly couple the supercontinuum beam to the liquid-core Bragg fiber with a 10× objective. The transmission spectra of the liquid-core Bragg fiber can be then analyzed by the Bragg fiber bundle spectrometer. Note that in the calibration, the illumination condition on the input-end facet of the fiber bundle should be identical to that in the following spectral characterization, which is critical to minimize the error in the spectral characterization process [25].

5.3. *Liquid-core Bragg fiber transmission measured by Bragg fiber bundle spectrometer*

The NaCl solutions of the same concentrations as discussed in Section 3 are used to characterize the sensing system that includes a fiber bundle spectrometer. The transmission spectra of the liquid-core Bragg fiber measured by the Bragg fiber bundle spectrometer is shown in Fig. 7(a). As a reference, we also measure the liquid-core Bragg fiber transmission by directly coupling it to a conventional grating monochromator (Fig. 7(b)). For the ease of comparison, the spectra measured both by the Bragg fiber bundle spectrometer and by the grating monochromator are normalized to 1. Since the spectra reconstructed by the fiber bundle spectrometer and measured by the grating monochromator are relatively wide, we, therefore, calculate the center position of a transmission peak by averaging the corresponding wavelengths where the normalized intensities are above 0.95.

In Fig. 7(c), we compare the shifts of transmission peaks measured by both the Bragg fiber bundle spectrometer and the grating monochromator. The transmission peak shifts also feature linear dependence with respect to the variations in the core RI of the Bragg fiber. Experimental sensitivity of the liquid Bragg fiber sensor is ~1100 nm/RIU measured by the grating monochromator and is ~1050 nm/RIU measured by the Bragg fiber spectrometer. Note that in both measurements presented in Fig. 7, the spectra shifts (see Fig. 7(c)) are marginally smaller than those shown in Fig. 4. This is likely due to the fact that during the measurements (including the calibration measurements) for Fig. 7, the Bragg fiber is kept straight in order to reduce the propagation loss of the liquid-core fiber and then increase the signal-to-noise ratio of the measurements. Therefore, many high-order modes, which are less sensitive to variations in RI of the fiber core, can propagate through the fiber, thus resulting in smaller spectral shifts. However, in the measurements for Figs. 3 and 4, signal-to-noise degradation is not a critical issue, since we use a more sensitive single-pixel detector for spectral interrogation as compared to the CCD detector used in the Bragg fiber spectrometer. Consequently, we coil the Bragg fiber piece as a 10 cm diameter circle in order to strip out high-order modes, thus leading to stronger spectral shifts.

6. Drawing of PBG fiber bundles

Finally, we demonstrate a two-stage drawing technique suitable for industrial-strength production of the Bragg fiber bundles. Briefly, this technique comprises two steps. Firstly, we fabricate a Bragg fiber perform by the "co-rolling" method [34] and draw it into the canes of different diameters ranging between 1 and 2 mm. Secondly, we bundle these canes inside a supercladding tube, and draw the structure into the final Bragg fiber bundle. The two-stage drawing technique, in principle, enables fabrication of smaller fiber bundles that include a large number of Bragg fibers featuring complimentary spectral transmission windows (Fig. 8). We are currently working on the perfection of the two-stage drawing technique in order to draw Bragg fiber bundles with reduced outer diameters, which eventually enables a fiber bundle to be directly spliced with a single HC Bragg fiber.

7. Conclusions

We report a liquid-core low-RI-contrast Bragg fiber sensor for liquid RI detection. The sensor operates on a resonant sensing mechanism in which the transmission spectrum of a Bragg fiber shifts in response to changes in RIs of liquid analytes filling in the fiber core. Both theoretical simulations and experimental measurements are carried out to verify the resonant sensing mechanism. The experimental sensitivity of the sensor is ~1400 nm/RIU, which is comparable to those of surface plasmon resonance sensors [35] and other MOF-based sensors. Besides, we also conclude that the sensitivity of a liquid-core Bragg fiber sensor is generally independent on the fiber length.

Moreover, we demonstrate the integration of a Bragg fiber bundle spectrometer in the liquid-core Bragg fiber sensor system for spectral acquisition, which could potentially lead to significant cost-savings and increased sensing speed by forgoing a traditional grating-based spectrometer. To the best of our knowledge, it is the first time that a fiber-optic sensor is proposed that simultaneously use all hollow- and solid-core PBG fibers to physically hold and spectrally probe liquid analytes. Finally, we propose a two-stage drawing technique for the fabrication of solid-core Bragg fiber bundle spectrometers. This technique results in integrated Bragg fiber bundles with smaller diameters, which could also allow their direct splicing with a HC Bragg fiber in order to enable a highly compact, sensitive, low-cost, all-fiber solution of liquid RI sensing.

References

[1] R. Manor, A. Datta, I. Ahmad, M. Holtz, S. Gangopadhyay, T. Dalls, Microfabrication and characterization of liquid core waveguide glass channels coated with Teflon AF, IEEE Sens. J. 3 (2003) 687.
[2] C. Ma, B. Scott, G. Pickrell, A. Wang, Porous capillary tubing waveguide for multigas sensing, Opt. Lett. 35 (2010) 315.
[3] V. Benoit, M.C. Yappert, Effect of capillary properties on the sensitivity enhancement in capillary/fiber optical sensors, Anal. Chem. 68 (1996) 183–188.
[4] J. Sun, C.C. Chan, Photonic bandgap fiber for refractive index measurement, Sens. Actuators B 128 (2007) 46–50.
[5] H.F. Xuan, W. Jin, J. Ju, H.L. Ho, M. Zhang, Y.B. Liao, Low-contrast photonic bandgap fibers and their potential applications in liquid-base sensors, in: Third European Workshop on Optical Fibre Sensors, Proc. SPIE 6619 (2007) 661936.
[6] K.J. Rowland, S. Afshar, V.A. Stolyarov, Y. Fink, T.M. Monro, Spectral properties of liquid-core Bragg fibers, in: Conference on Lasers and Electro-Optics/International Quantum Electronics Conference, Maryland, CThE2, 2009.
[7] L. Rindorf, P.E. Hoiby, J.B. Jensen, L.H. Pedersen, O. Bang, O. Geschke, Towards biochip using microstructured optical fiber sensors, Anal. Bioanal. Chem. 385 (2006) 1370–1375.
[8] J.B. Jensen, L.H. Pedersen, P.E. Hoiby, L.B. Nielsen, T.P. Hansen, J.R. Folkenberg, J. Riishede, D. Noordegraaf, K. Nielsen, A. Carlsen, A. Bjarklev, Photonic crystal fiber based evanescent-wave sensor for detection of biomolecules in aqueous solutions, Opt. Lett. 29 (2004) 1974.
[9] Y. Han, M.K. Khaing, Y. Zhu, L. Xiao, M.S. Demohan, W. Jin, H. Du, Index-guiding liquid-core photonic crystal fiber for solution measurement using normal and surface-enhanced Raman scattering, Opt. Eng. 47 (2008) 040502.
[10] Y. Zhang, C. Shi, C. Gu, L. Seballos, J.Z. Zhang, Liquid core photonic crystal fiber sensor based on surface enhanced Raman scattering, Appl. Phys. Lett. 90 (2007) 193504.
[11] J. Irizsar, J. Dinglasan, J.B. Goh, A. Khetani, H. Anis, D. Anderson, C. Goh, A.S. Helmy, Raman spectroscopy of nanoparticles using hollow-core photonic crystal fibers, IEEE J. Select. Top. Quant. Electron. 14 (2008) 1214.
[12] X. Yang, C. Shi, D. Wheeler, R. Newhouse, B. Chen, J.Z. Zhang, C. Gu, High-sensitivity molecular sensing using hollow-core photonic crystal fiber and surface-enhanced Raman scattering, J. Opt. Soc. Am. A 27 (2010) 977.
[13] C. Charlton, B. Temelkuran, G. Dellemann, B. Mizaikoff, Midinfrared sensors meet nanotechnology: trace gas sensing with quantum cascade lasers inside photonic band-gap hollow waveguides, Appl. Phys. Lett. 86 (2005) 194102.
[14] L.C. Shi, W. Zhang, J. Jin, Y. Huang, J.D. Peng, Hollow-core Bragg fiber and its application in trace gas sensing, optical sensors and biophotonics II, in: Proceedings of SPIE-OSA-IEEE Asia Communications and Photonics, SPIE, vol. 7990, 2011, p. 799008.
[15] T. Ritari, J. Tuominen, H. Ludvigsen, J.C. Petersen, T. Sorensen, T.P. Hansen, H.R. Simonsen, Gas sensing using air-guiding photonic bandgap fibers, Opt. Express 12 (2004) 4080.
[16] Y.L. Hoo, S. Liu, H.L. Ho, W. Jin, Fast response microstructured optical fiber methane sensor with multiple side-openings, IEEE Photonic Technol. Lett. 22 (2010) 296.
[17] A.M. Cubillas, M. Silva-lopez, J.M. Lazaro, O.M. Conde, M.N. Petrovich, J.M. Lopez-Higuera, Methane detection at 1670-nm band using a hollow-core photonic bandgap fiber and a multiline algorithm, Opt. Express 15 (2007) 17570.
[18] A.M. Cubillas, J.M. Lazaro, M. Silva-Lopez, M.N. Petrovich, J.M. Lopez-Higuera, Methane sensing at 1300 nm band with hollow-core photonic bandgap fibre as gas cell, Electron. Lett. 44 (2008) 403.
[19] M.P. Buric, K.P. Chen, J. Falk, S.D. Woodruff, Enhanced spontaneous Raman scattering and gas composition analysis using a photonic crystal fiber, Appl. Opt. 47 (2008) 4255.
[20] M.P. Buric, K.P. Chen, J. Falk, S.D. Woodruff, Improved sensitivity spontaneous Raman scattering multi-gas sensor, CLEO/IQEC 2009, CThI6.
[21] S.H. Aref, R. Amezcua-Correac, J.P. Carvalho, O. Frazao, J.L. Santos, F.M. Araujo, H. Latifi, F. Farahi, L.A. Ferreira, J.C. Knight, Spectral characterization of a photonic bandgap fiber for sensing applications, Appl. Opt. 49 (2010) 1870.
[22] G. Kim, T. Cho, K. Hwang, K. Lee, K.S. Lee, Y.G. Han, S.B. Lee, Strain and temperature sensitivities of an elliptical hollow-core photonic bandgap fiber based on Sagnac interferometer, Opt. Express 17 (2009) 2481.
[23] H. Xuan, W. Jin, M. Zhang, J. Ju, Y. Liao, In-fiber polarimeters based on hollow-core photonic bandgap fibers, Opt. Express 17 (2009) 13246.
[24] M. Skorobogatiy, Resonant bio-chemical sensors based on Photonic Bandgap waveguides and fibers, in: M. Zourob, L. Akhlesh (Eds.), Optical Guided-wave Chemical and Biosensors II, Springer, Berlin, Heidelberg, 2010, pp. 43–72.
[25] H. Qu, B. Ung, I. Syed, N. Guo, M. Skorobogatiy, Photonic bandgap fiber bundle spectrometer, Appl. Opt. 49 (2010) 4791.
[26] E. Pone, C. Dubois, N. Guo, A. Dupuis, F. Boismenu, S. Lacroix, M. Skorobogatiy, Drawing of the hollow all-polymer Bragg fibers, Opt. Express 14 (2006) 5838.
[27] M. Skorobogatiy, Efficient antiguiding of TE and TM polarizations in low-index core waveguides without the need for an omnidirectional reflector, Opt. Lett. 30 (2005) 2991.
[28] S.G. Johnson, M. Ibanescu, M. Skorobogatiy, O. Weiseberg, T.D. Engeness, M. Soljacic, S.A. Jacobs, J.D. Joannopoulos, Y. Fink, Low-loss asymptotically singe-mode propagation in large core omniguide fibers, Opt. Express 9 (2001) 748.
[29] W.M. Haynes, CRC Handbook of Chemistry and Physics, 91st ed., CRC Press, Boca Raton, FL, 2010, pp. 8–71.
[30] J.M. Sullivan, M.S. Twardowski, J.R.V. Zaneveld, C.M. Moore, A.H. Barnard, P.L. Donaghay, B. Rhoades, Hyperspectral temperature and salt dependence of absorption by water and heavy water in the 400–750 nm spectral range, Appl. Opt. 45 (2006).
[31] M.H. Frosz, A. Stefani, O. Bang, Highly sensitive and simple method for refractive index sensing of liquid in microstructured optical fibers using four-wave mixing, Opt. Express 19 (2011) 10471.
[32] L. Rindorf, O. Bang, Highly sensitive refractometer with a photonic-crystal-fiber long-period grating, Opt. Lett. 33 (2008) 563.
[33] D.K.C. Wu, B.T. Kuhlmey, B.J. Eggleton, Ultrasensitive photonic crystal fiber refractive index sensor, Opt. Lett. 34 (2009) 322.
[34] Y. Gao, N. Guo, B. Gauvreau, M. Rajabian, O. Skorobogata, E. Pone, O. Zabeida, L. Martinu, C. Dubois, M. Skorobogatiy, Consecutive solvent evaportation and co-rolling technique for polymer multilayer hollow fiber perform fabrication, J. Mater. Res. 21 (2006) 2246.
[35] A. Hassani, M. Skorobogatiy, Design criteria for microstructured-optical-fiber-based surface-plasmon-resonance sensors, J. Opt. Soc. Am. B 24 (2007) 1423.

Biographies

Hang Qu has received his B.Sc. and M.Sc. in physics from Jilin University in 2005 and 2007, respectively. He is currently working towards a Ph.D. in engineering physics at Ecole Polytechnique de Montreal. His current fields of interest include photonic bandgap fiber sensing, capillary fiber sensing, microstructured-fiber-based devices.

Bora Ung has received his BE and M.Sc. in engineering physics from Laval University in 2004 and 2007, respectively. He is currently working towards a Ph.D. in engineering physics at Ecole Polytechnique de Montreal. He is the recipient of a SPIE 2011 Scholarship in Optics & Photonics. His current fields of interest include nonlinear fiber optics and waveguides, fiber-based devices, nano-optics, plasmonics, infrared and terahertz science.

Dr. Mathieu Roze has received his Ph.D. in chemistry from University of Rennes 1 in 2009. He works as a postdoctoral research fellow at Ecole Polytechnique de Montreal since 2010. His fields of interest include fabrication of microstructured optical fiber, soft glass processing.

Dr. Maksim Skorobogatiy has received his B.Sc. degree in physics from Rochester Institute of Technology, Rochester, USA (1995); M.Sc. in physics from McGill University, Montréal, Canada (1997); M.Sc. in electrical engineering and computer science from Massachusetts Institute of Technology (MIT), Cambridge, USA (2000); Ph.D. in physics also from MIT in 2001. During 2001–2003 he was heading a theory and simulations group at MIT startup OmniGuide Inc., where he was working on commercialization of the hollow photonic bandgap fiber technology for delivery of high power laser beams. Since 2003, he is an associate professor and a Canada Research Chair in Micro- and Nano-Photonics at Ecole Polytechnique de Montréal/University de Montréal, Canada. His current fields of interest include design and fabrication of photonic crystal fibers for sensing and telecommunications, as well as the general fields of plasmonics, and nano-photonics.